

CO₂ fixation into carbon nanofibres using electrochemical-thermochemical tandem catalysis

Z. Xie

To be published in "Nature Catalysis"

January 2024

Chemistry Department
Brookhaven National Laboratory

U.S. Department of Energy
USDOE Office of Science (SC), Basic Energy Sciences (BES)

Notice: This manuscript has been authored by employees of Brookhaven Science Associates, LLC under Contract No. DE-SC0012704 with the U.S. Department of Energy. The publisher by accepting the manuscript for publication acknowledges that the United States Government retains a non-exclusive, paid-up, irrevocable, world-wide license to publish or reproduce the published form of this manuscript, or allow others to do so, for United States Government purposes.

DISCLAIMER

This report was prepared as an account of work sponsored by an agency of the United States Government. Neither the United States Government nor any agency thereof, nor any of their employees, nor any of their contractors, subcontractors, or their employees, makes any warranty, express or implied, or assumes any legal liability or responsibility for the accuracy, completeness, or any third party's use or the results of such use of any information, apparatus, product, or process disclosed, or represents that its use would not infringe privately owned rights. Reference herein to any specific commercial product, process, or service by trade name, trademark, manufacturer, or otherwise, does not necessarily constitute or imply its endorsement, recommendation, or favoring by the United States Government or any agency thereof or its contractors or subcontractors. The views and opinions of authors expressed herein do not necessarily state or reflect those of the United States Government or any agency thereof.

CO₂ fixation into carbon nanofibers using electrochemical-thermochemical tandem catalysis

Zhenhua Xie^{1,2,†}, Erwei Huang^{2,†}, Samay Garg¹, Sooyeon Hwang³, Ping Liu^{2*}, Jingguang G. Chen^{1,2*}

¹Department of Chemical Engineering, Columbia University, New York, 10027, USA.

²Chemistry Division, Brookhaven National Laboratory, Upton, 11973, USA.

³Center for Functional Nanomaterials, Brookhaven National Laboratory, Upton, 11973, USA.

*Corresponding authors. Emails: pingliu3@bnl.gov; jgchen@columbia.edu.

†These authors contributed equally to this work.

Abstract

Carbon dioxide (CO₂) fixation into value-added solid carbon such as carbon nanofiber (CNF) for longer-term storage represents a promising avenue for achieving net-negative carbon emissions. However, directly converting CO₂ to CNF via thermocatalytic approaches faces thermodynamic constraints, while electrocatalytic methods typically lead to amorphous carbon with limited yields or require energy-intensive conditions (>720 °C). Herein, we present an electrocatalytic-thermocatalytic tandem strategy for CNF production, which circumvents the aforementioned thermodynamic limitations by integrating the co-electrolysis of CO₂ and water into syngas (CO and H₂) with a subsequent thermochemical process at relatively mild conditions (370-450 °C, 1 atm), yielding CNF at a high production rate (*avg.* 2.5 g_{carbon} g_{metals}⁻¹ h⁻¹). The coordinated actions of FeCo alloy and extra metallic Co were ascertained optimal to enhance the dissociative activation of syngas and favor the carbon-carbon bond formation to produce CNF. This tandem strategy opens a door to leverage renewable energy for decarbonizing CO₂ into valuable solid carbon products while producing renewable H₂.

Introduction

The global climate crisis has become a major concern due to the emissions of anthropogenic carbon dioxide (CO₂).^{1,2} CO₂ mitigation is strongly demanded in hard-to-abate sectors, such as the cement, steel, and chemical industries. Carbon capture, utilization, and storage (CCUS) has been identified as one promising strategy to achieve net zero-emissions.³ Capturing CO₂ for underground storage has been discussed for decades, however, engineering challenges and risks of leakage have hampered implementation. In parallel, various approaches to CO₂ conversion, including thermochemical,⁴⁻⁶ electrochemical,⁷⁻¹⁰ photochemical,¹¹ plasma,^{12,13} biological,^{14,15} and hybrid^{16,17} processes, have been advanced to produce a variety of value-added chemicals (*e.g.*, syngas, alkanes, olefins, aromatics, and oxygenates) or fuels (*e.g.*, gasoline, diesel, and jet fuels). However, most of the resulting gaseous or volatile products are eventually released to atmosphere as CO₂ after consumption, thereby making it difficult to achieve negative CO₂ emissions. Moreover, the vast scale of carbon emissions, estimated to be 40 Gt CO₂ annually, presents challenges in discovering breakthrough technologies to effectively mitigate CO₂ emissions.^{18,19}

CO₂ valorization into non-volatile or solid products that are suitable for longer-term storage is expected to play a crucial role in achieving negative emissions as the world shifts toward renewable energy sources. Solid carbon materials such as carbon nanotube (CNT), carbon nanofiber (CNF), graphene, and carbon black have gained interests in a wide range of industrial sectors with a > \$30 billion market size due to their unique structural, mechanical, electrical, thermal, optical, and chemical properties.²⁰ However, thermodynamic constraints pose challenges for direct CO₂-to-solid carbon conversion via thermocatalytic methods. At present, there have been only a limited number of reports on CO₂ valorization into solid carbon products: the electrochemical reduction of CO₂ with Galinstan-based liquid metals, which produces solid carbons, but in amorphous morphology and with low yield and/or low current density (<10 mA cm⁻²);²¹⁻²³ alternatively, CO₂ electrolysis in molten lithium (Li) bicarbonate was introduced to synthesize CNT or CNF, but it requires high temperatures (>720 °C) and competes for the limited Li supplies with the battery industry.^{24,25} As such, approaches that allow for large-scale conversion of CO₂ into value-added solid carbon products at mild conditions, in facile integration with renewable energy and good compatibility with existing infrastructure, will open a door for negative carbon emissions and economically and technically facilitate commercial decarbonization.

To achieve this, herein we propose an electrochemical-thermochemical tandem strategy that circumvents thermodynamic limitations (ΔG_{eq}). This process firstly electrolyzes CO₂ and water into syngas (CO and H₂), followed by thermochemical upgrading into CNF at relatively low temperatures (370-450 °C) and ambient pressure. Moreover, H₂ can be obtained as a renewable byproduct. Experimental and theoretical insights reveal that the synergistic actions between FeCo alloy and extra metallic Co serve as the optimal catalyst for the CNF production. Furthermore, proof-of-principle demonstrations of product separation involving metal recycling and assessment of energy costs and CO₂ emissions reveal the promising applicability of the tandem strategy.

Results

CNF production from thermal conversion of syngas at mild conditions

In addition to the wide range of applications in power generation and storage, electronic devices and gas storage,²⁶ CNF has been shown to reinforce composites such as cements by preventing nanocracks and filling pores in the cementitious matrix,^{27,28} thus presenting an opportunity for permanent fixation of large amounts of carbon into worldwide building materials.²⁹ However, the conventional synthesis methods of pyrolysis or catalytic decomposition of carbon precursors

typically require high temperatures ($>700\text{ }^{\circ}\text{C}$) and often at elevated pressures, representing an energy-intensive process.³⁰ Thus, a key challenge is to produce appreciable amounts of CNF from CO_2 with lower energy consumption, preferably powered by renewable energy.

The reactions of $2\text{CO} \rightarrow \text{C(s)} + \text{CO}_2$ (*i.e.*, Boudouard reaction, **R1**) and $\text{CO} + \text{H}_2 \rightarrow \text{C(s)} + \text{H}_2\text{O}$ (**R2**) have been identified for carbon formation. However, they are typically treated as undesired coking reactions that are responsible for catalyst deactivation and reactor blockage in commercial processes such as Fischer-Tropsch (F-T) synthesis and steam methane reforming.^{31,32} Intriguingly, both **R1** and **R2** are highly exothermic (Fig. 1a) and therefore thermodynamically favorable at low temperatures. **R1** is energetically more preferred than **R2** with a higher equilibrium conversion of CO (*e.g.*, 94.1% vs. 75.3% at $400\text{ }^{\circ}\text{C}$, Fig. 1b), while **R2** exhibits a higher C(s) yield than **R1** (*e.g.*, 75.3% vs. 47.3% at $400\text{ }^{\circ}\text{C}$). In the presence of both pathways, CO conversion can be retained at above 90% up to $450\text{ }^{\circ}\text{C}$, followed by rapid decreases at higher temperatures; in parallel, the C(s) amount or yield gradually decreases (*e.g.*, 66.7% at $400\text{ }^{\circ}\text{C}$) and becomes nearly negligible at above $600\text{ }^{\circ}\text{C}$ (Fig. 1c). It is noted that the practical equilibrium C(s) yield is likely lower considering the potentially competitive reactions of CO methanation ($\text{CO} + 3\text{H}_2 \rightarrow \text{CH}_4 + \text{H}_2\text{O}$), water-gas shift (WGS, $\text{CO} + \text{H}_2\text{O} \rightarrow \text{H}_2 + \text{CO}_2$), and/or carbon gasification ($\text{C(s)} + 2\text{H}_2 \rightarrow \text{CH}_4$). Thus, catalysts with high selectivity to C(s) should be employed to maximize the solid carbon products; moreover, to balance the thermodynamics and kinetics of solid carbon production, optimal temperatures appear to be between $400\text{--}450\text{ }^{\circ}\text{C}$.

Although CNF formation is a complex process, it is primarily governed by three successive steps: dissociative adsorption of carbon precursors at the gas/metal interface, carbon diffusion through the bulk of metal catalysts or migration along the catalyst surface, and carbon precipitation and growth at the catalyst/solid carbon interface.^{26,33} Among potential catalysts, Fe, Co, Ni, and Ru have been recognized as highly effective metals for the dissociative adsorption of CO and H_2 in traditional F-T synthesis. However, Fe exhibits higher WGS activity, Ni favors methanation more than Co, and Ru is limited by its high cost. Bimetallic catalysts have been shown to optimize reactant activation and alter selectivity.^{6,33,34} Therefore, supported non-precious FeCo bimetallic catalysts are employed in this study to achieve CNF formation at relatively mild temperatures and ambient pressure.

Catalyst weight gain (CWG) relative to the initial catalyst loading is employed as an initial indicator of solid carbon formation after reaction. The elemental composition effect (Fig. 1d, Supplementary Figs. 1-2) is assessed by varying the Fe/Co ratio from 9/0 to 6/3, 4.5/4.5, 3/6, and 0/9 while keeping the total moles of metal elements constant. The highest CWG (265 mg) is obtained at the Fe/Co ratio of 3/6, showing the synergistic effect of alloying Fe and Co for catalyzing solid carbon production. Solid carbon production can be further enhanced to 350 mg with higher metal loading ($\text{Fe}_6\text{Co}_{12}$) while keeping the same Fe/Co atomic ratio. It is noted that with CO feed only ($\text{CO}/\text{H}_2/\text{N}_2=3/0/7\text{ ml min}^{-1}$), rapid deactivation of $\text{Fe}_3\text{Co}_6/\text{CeO}_2$ is observed with a small CWG (40 mg) due to carbon encapsulation (Supplementary Fig. 3). The necessity of H_2 in CNF formation is corroborated by an increased CWG when co-feeding H_2 ($3/3/4\text{ ml min}^{-1}$ in Fig. 1e, Supplementary Fig. 4). Moreover, the observation of CWG under various feed composition ratios highlights the tolerance of the FeCo catalysts for CNF formation using H_2/CO mixtures with a relatively wide range of feed compositions. The CWG also increases with the flow rates of $\text{CO}/\text{H}_2/\text{N}_2$ (Supplementary Fig. 5). A comparison of reduction and reaction temperatures (Supplementary Figs. 6-8) reveal optimal carbon formation at around $450\text{ }^{\circ}\text{C}$ (Fig. 1f, Supplementary Fig. 8), in line with the thermodynamic analysis of the reaction temperature window. Although both CO and H_2 show a gradual decrease in conversion after being on stream

for 30 min, primarily due to the diminishing methanation reaction toward CH₄, the carbon fixation rate remains stable within about 5 h (Fig. 1g, Supplementary Fig. 9) as evidenced by the constant carbon balance. A gram-level CWG (1.7 g) can be obtained within ~37 h (Supplementary Fig. 10). Additionally, the role of the CeO₂ support in promoting solid carbon formation is highlighted by the lower CWG values observed over its γ -Al₂O₃, SiO₂, and MCM-41 supported counterparts (Supplementary Fig. 11). It is noted that the metal-CeO₂ interface in activating reactants is limited according to the density function theory (DFT) calculations (see Supplementary Note 1, Supplementary Fig. 12 and Supplementary Table 1). The enhanced performance of CeO₂-supported catalysts toward solid carbon formation is primarily due to the more facile reducibility of Fe and Co oxides supported on CeO₂ than the other supports, as corroborated by the temperature-programmed reduction (TPR) measurements (Supplementary Fig. 6).

Transmission electron microscopy (TEM) imaging of the spent Fe₃Co₆/CeO₂ catalyst (Fig. 1h, Figs. S13-S14) reveals the formation of CNF with diameters of 20-30 nm and lengths of hundreds of nm to a few μ m. The formation of CNF primarily follows a tip-growth mechanism³⁵, which pushes the metal nanoparticles away from the support and places them within the *tip* of CNF (Fig. 1i), as further confirmed by the combined high-angle annular dark field (HAADF) imaging and energy-dispersive X-ray spectroscopy (EDS) mapping of C, Fe, Co, and Ce (Fig. 1j, Supplementary Tables 2-3). Analysis using Raman spectroscopy (Supplementary Fig. 15 and Supplementary Table 4) suggests a CNF purity of ~90% and crystallinity of ~80% relative to the commercial CNF reference, consistent with the presence of a minor fraction of amorphous carbon agglomerates seen in the TEM image (Fig. 1h). In addition, the EDS measurements (Supplementary Fig. 16, Supplementary Table 5) conducted over the resulting CNFs reveal a high elemental purity as evidenced by the atomic compositions (C: ~99.0%, O: <1.0%, Fe, Co, and Ce: <0.2%). Co₉/CeO₂ follows a similar *tip*-growth mechanism of CNF (Supplementary Fig. 17). In contrast, the spent Fe₉/CeO₂ catalyst shows predominantly amorphous carbon species (Supplementary Fig. 18), confirming the synergistic effect of the Fe-Co bimetallic catalysts.

Structural properties of catalysts responsible for CNF formation

To unravel the structures that are responsible for the synergistic interaction of Fe and Co in CO and H₂ dissociative activation and C-C backbone formation, *in situ* powder X-ray diffraction (XRD) and *in situ* X-ray absorption fine structure (XAFS) spectroscopy are utilized. Co₃O₄ ($2\theta_{(311)}=14.62^\circ$, $2\theta_{(222)}=15.28^\circ$, and $2\theta_{(400)}=17.66^\circ$, Fig. 2a) is observed to be dominant over the fresh Co₉/CeO₂ catalyst, which is reduced to CoO ($2\theta_{(111)}=14.42^\circ$ and $2\theta_{(200)}=16.67^\circ$) first before being fully reduced to metallic Co with the co-existence of *fcc* ($2\theta_{(111)}=17.37^\circ$) and *hcp* ($2\theta_{(100)}=16.39^\circ$) phases. The reduction behavior of Co₃O₄ to CoO is observed similarly in the Fe_xCo_y/CeO₂ bimetallic catalysts but with diminished peak intensity as the Fe/Co ratio increases from 3/6 to 4.5/4.5 and 6/3. At 500 °C reduction, Fe₃Co₆/CeO₂ shows the dominance of a *bcc* Fe-Co alloy phase ($2\theta_{(110)}=17.67^\circ$) with a minor amount of *fcc* Co phase ($2\theta_{(111)}=17.35^\circ$). As for Fe₉/CeO₂, a *bcc* Fe phase ($2\theta_{(110)}=17.48^\circ$) forms after 700 °C reduction. Upon exposure to the CO and H₂ stream at 450 °C, the metallic Fe phase vanishes instantly, which is attributed to fragmentation, a well-documented phenomenon caused by carbon supersaturation within the bulk of metal particles.^{36,37} A similar phenomenon was observed over Fe₃Co₆/SiO₂ (Supplementary Fig. 19). In contrast, for Fe₃Co₆/CeO₂ the alloy phase remains stable under reaction conditions, indicating the stabilizing effect of Co on the alloy phase. Furthermore, the presence of additional metallic Co in Fe₃Co₆/CeO₂, which results in a higher CWG (265 mg) than Fe_{4.5}Co_{4.5}/CeO₂ (190 mg) and Co₉/CeO₂ (120 mg), suggests that the co-existence of FeCo alloy and extra Co is likely

the optimal combination for CO and H₂ dissociative activation and C-C backbone formation as supported by the DFT calculations.

The *in situ* Fe and Co K-edge X-ray absorption near-edge spectroscopy (XANES) results (Figs. 2b, 2e) indicate that Fe₂O₃ and Co₃O₄ over Fe₃Co₆/CeO₂ are reduced to metallic state at 500 °C. The Fe-Co alloy formation in Fe₃Co₆/CeO₂ is further validated by the Fe and Co K-edge extended X-ray absorption fine structure (EXAFS) features in both *k*-space (Figs. 2c, 2f) and *R* space (Figs. 2d, 2g), which resemble those of a *bcc* Fe foil rather than an *fcc* Co foil,^{38,39} consistent with the *in situ* XRD results. After exposure to CO and H₂ at 450 °C for about 5 h, both Fe and Co are slightly oxidized but with different oxidative features, in particular the pre-edge peak (Figs. 2b, 2e, Supplementary Fig. 20), from their oxide standards (FeO, Fe₃O₄, Fe₂O₃, CoO, and Co₃O₄). This is likely due to metal-C bond formation,⁴⁰ as revealed by the EXAFS fittings (Supplementary Fig. 21 and Supplementary Table 6) where the average coordination number (CN) of Co-C bond is 0.8 with a bond distance of 1.80 Å. Although the formation of a minor amount of metal carbides is not observed by XRD, likely due to the lack of long-range ordering, they may affect the activation of CO and H₂ and the stability of catalysts as supported by the DFT calculations.

Mechanistic insights into syngas activation and C-C bond formation

DFT studies (Fig. 3, Supplementary Figs. 23-44, Supplementary Tables 7-14) were performed to enhance insights into the structures and catalytic behaviors observed experimentally, where *bcc* FeCo was selected to model the Fe-Co alloy according to the *in situ* XRD measurement (Fig. 2a). The thermodynamic analysis (Fig. 3a) demonstrates that under the reaction conditions of both **R1** and **R2**, *bcc* Fe is highly unstable and prone to form Fe₃C, while *hcp* Co prefers to stay as metallic. By combining Co and Fe, the FeCo alloy displays a stability as high as Co with the metallic phase being favored. Introducing H₂ along with CO gas also helps stabilize the metallic phase for Fe, Co and FeCo due to the H₂-induced increase in chemical potential change of C species ($\Delta\mu_C^R$) at the equilibrium states (Supplementary Fig. 28).

To compare the reaction pathways, the most stable orientation is considered for the monometallic and bimetallic surfaces, *i.e.*, Fe(110), Co(0001) and FeCo(110). Upon exposure to CO only (Fig. 3b, Supplementary Fig. 29), the Fe(110) surface is highly reactive in term of adsorption (adsorption energy, $E_{\text{ads}}=-2.17$ eV) and dissociation (reaction energy, $\Delta E=-0.89$ eV, activation barrier, $E_a=1.18$ eV). In comparison, the Co(0001) surface binds CO more weakly ($E_{\text{ads}}=-1.86$ eV) with a higher barrier for C-O bond cleavage ($\Delta E=0.82$ eV, $E_a=2.28$ eV). The FeCo(110) alloy surface exhibits a comparable reactivity to Fe(110) toward adsorption ($E_{\text{ads}}=-2.09$ eV) and dissociation ($\Delta E=-0.19$ eV, $E_a=1.64$ eV) of CO (Fig. 3b), where both Fe and Co sites exposed on the surface participate in CO dissociation to stabilize the dissociated *C and *O fragments.

Once *C is formed from CO dissociation, the initial C-C bond formation toward the growth of CNF is unfavorable on Fe(110) ($\Delta E=0.65$ eV, $E_a=1.43$ eV) (Fig. 3c, Supplementary Table 7). Instead, the conversion of Fe to Fe₃C is preferred under reaction conditions (Fig. 3a, Supplementary Note 2), which likely reduces activity due to difficulty in C-O bond activation ($E_a=2.49$ eV, Supplementary Fig. 30 and Supplementary Table 8). In comparison, the C-C bond formation is more preferred or at least comparable to the reverse decomposition on both Co(0001) ($\Delta E=-0.62$ eV, $E_a=0.96$ eV) and FeCo(110) ($\Delta E=0.26$ eV, $E_a=1.13$ eV) surfaces (Fig. 3c, Supplementary Figs. 31-32). Furthermore, compared to Co alone, Co alloyed with Fe likely facilitates the CO dissociation (FeCo: $\Delta E=-0.19$ eV, $E_a=1.64$ eV; Co: $\Delta E=0.82$ eV, $E_a=2.28$ eV), but with a reduced rate for C-C bond formation. Thus, the coexistence of Co with FeCo likely takes advantage of both systems, being able to allow CO dissociation to produce *C on the FeCo

alloy, while facilitating the C-C coupling of the produced *C species and CNF growth on Co by the facile diffusion of *C species from FeCo to Co (see Supplementary Note 3, Supplementary Fig. 33 and Supplementary Table 9). This is consistent with experimental observation of higher CWG values on FeCo catalysts with higher Co/Fe ratios (Fig. 1d) and the corresponding detection of the co-existence of FeCo and metallic Co by *in situ* XRD (Fig. 2).

As observed experimentally, a trend going from Fe < Co \approx FeCo in increasing activity during CNF formation was observed for the removal of *O fragments from *CO dissociation, which can occur via the formation of either CO₂ by reacting with neighboring *CO via the Boudouard reaction (Fig. 3d, Supplementary Fig. 34) or H₂O by reacting with *H from H₂ dissociation (Fig. 3e, Supplementary Figs. 35-37, Supplementary Table 7). In both cases, FeCo(110) and Co(0001) can enable more facile removal of *O than Fe. Note that the hydrogenation of *OH species to *H₂O on both FeCo (E_a=1.74 eV) and Co (E_a=1.50 eV) requires overcoming a higher energy barrier than the formation of *CO₂ (Fig. 3, Supplementary Table 7), likely indicating a dominant Boudouard reaction for CNF formation as observed experimentally (Fig. 1). In addition, the *H-assisted conversion of CO to *HCO or *COH is thermodynamically less favorable compared to the direct CO dissociation (Fig. 3b, Supplementary Table 10), which also ensures the preference for **R1** over **R2**.

Overall, the formation of the FeCo alloy is advantageous over Fe and Co alone in CO/H₂ activation, being as active as that of Fe to facilitate the direct CO dissociation, but still moderately enough to enable facile *O removal and C-C bond formation as that of Co toward the growth of CNF. In addition, the FeCo metallic phase, which is essential for initiating the CNF growth, is stable enough as that of Co to prevent carbide formation under reaction conditions. The catalytic promoting effect of FeCo strongly depends on interplay between the ensemble and electronic effects (see Supplementary Note 4, Supplementary Figs.38-44, Supplementary Tables 11-14),^{41,42} which effectively promotes the Boudouard reaction and initiates the CNF growth.

CO₂ to CNF via the electrochemical-thermochemical tandem process

The successful synthesis of CNF from CO and H₂ over the FeCo catalysts suggests that, in principle, any process capable of producing syngas with appropriate H₂/CO ratios can potentially be used to generate the feedstock to produce CNF (Fig. 1e, Supplementary Figs. 4-5). One promising method is the electrochemical CO₂ reduction reaction (CO₂RR) because it easily integrates with renewable electricity and can produce H₂/CO in controllable ratios at industrially relevant current densities (>1 A cm⁻²).^{7,8,43,44} We demonstrate an electrochemical-thermochemical tandem process for CNF production as illustrated in Fig. 4a. The tandem process starts with the co-electrolysis of CO₂ and H₂O at the cathode to produce CO via CO₂RR and H₂ via the hydrogen evolution reaction (HER), respectively, balanced by the oxygen evolution reaction (OER) at the anode.⁴⁵ The resulting cathodic products (CO and H₂) are subsequently fed into the thermochemical reactor to produce CNF via the **R1** and/or **R2** pathways.

HER is typically considered as an undesired competing reaction to CO₂RR;⁴⁶ however, the FeCo thermocatalyst is tolerant to—and in fact benefits from—the presence of H₂ (Supplementary Fig. 4), which allows for more flexibility in selecting CO₂RR catalysts and optimization of electrolyzer conditions, including the overpotential, electrolyte composition, ion exchange membrane, and electrolyte pH. We previously demonstrated that the *in situ* formation of β -phase Pd hydride over a Pd/C catalyst can provide a H₂/CO ratio between 1 and 2,⁴⁷ which can be fed into the thermochemical reactor for CNF production. We employ a 5 cm² zero-gap membrane electrode assembly (MEA) electrolyzer equipped with an anion exchange membrane and adopt

commercially available 10%, 20%, and 40%Pd/C catalysts immobilized on a gas diffusion layer. Under galvanostatic conditions, the current density is raised from -60 to -100, -150, and -200 mA cm⁻². As summarized in Supplementary Figs. 45-48, electrolysis using 10%Pd/C at -150 mA cm⁻² represents the optimal combination (see Supplementary Note 5) to integrate with the thermochemical reactor operating at 450 °C. Fig. 4b shows that a stable conversion of CO₂, in terms of both X_{total} (~78.5%) and X_{products} (~15.2%), is obtained at -150 mA cm⁻² within the 11 h of tandem process. As indicated by the carbon balance, the significant difference between X_{total} and X_{products} during the tandem process should not only stem from carbonation at the cathode and transport of (bi)carbonates toward the anode, but also from carbon fixation as a solid. H₂ is the dominant product (~0.4 mol g_{Pd/C}⁻¹ h⁻¹) in the gas phase followed by CO, while the side hydrogenation product, CH₄, is largely suppressed. The resulting spent Fe₃Co₆/CeO₂ catalyst shows 240 mg of CWG (Fig. 4e), corresponding to a production rate of *avg.* 2.5 g_{carbon} g_{metals}⁻¹ h⁻¹, and the TEM imaging (Fig. 4f) reveals the predominant formation of CNF. Accordingly, the Raman spectra (Supplementary Fig. 15 and Supplementary Table 4) suggest a nearly 100% purity and ~80% crystallinity relative to the commercial CNF reference; moreover, the EDS analysis (Supplementary Fig. 49 and Supplementary Table 15) confirms the prevalence of carbon, with impurities (e.g., O, Fe, Co, and Ce) being less than 1.0 atomic %. At a higher current density of -200 mA cm⁻² (Supplementary Fig. 48), a similar CWG of 250 mg was obtained with a higher H₂ productivity of ~0.7 mol g_{Pd/C}⁻¹ h⁻¹.

Fig. 4d shows that the CNF products are connected to the FeCo catalysts. For practical applications, it is important to separate the CNF from the catalysts and recycle the metals for subsequent reactions. As illustrated in Supplementary Fig. 50, we demonstrate a separation process including a sequence of steps involving ultrasonication, nitric acid leaching, centrifugation, and filtration, after which the separated catalysts are regenerated and reused for subsequent reactions. The spent FeCo sample is treated with nitric acid for 2, 5, and 12 h. The ICP analysis (Supplementary Table 16) indicates that ~70% of metals could be leached out after 2 h of treatment, while 5 and 12 h could leach out most of the metals (80-90%). Thus, a 5 h nitric acid treatment is used for subsequent regeneration experiments. Collected across various regions and scales, the TEM, scanning electron microscopy (SEM), and selected area electron diffraction (SAED) images (see Supplementary Note 6, Supplementary Figs. 51 and 52) reveal the presence of high-crystallinity CNF and the open CNF *tips* after the separation process, indicating efficient removal of metal ensembles within the *tip* through treatments like ultrasonication and nitric acid digestion. For catalyst regeneration, we either added new CeO₂ (Fe_xCo_y+CeO₂) or used some of the obtained solid products after separation (Fe_xCo_y+solids) to a concentrated solution containing iron and cobalt ions to achieve a similar metal loading as catalysts in the initial experiments. Supplementary Fig. 52a-b shows that the Fe_xCo_y+CeO₂ sample exhibits stable and similar CO and H₂ conversion compared to the initial Fe₆Co₁₂/CeO₂ catalyst within about 5 h, along with a comparable CWG (170 vs. 160 mg). TEM analysis (Supplementary Fig. 53c-d) reveals the formation of CNFs, similar to the fresh catalysts. The Fe_xCo_y+solids sample (Supplementary Fig. 54) shows relatively steady and lower conversion, in line with a lower CWG (114 mg). These results demonstrate the proof-of-principle of recycling and reusing the FeCo catalysts; future follow-up studies will further optimize the recycling and regeneration procedures.

As shown in Fig. 4b and Supplementary Fig. 48, the effluents from the tandem reactors mainly contain H₂, CO, CO₂, with a minor presence of H₂O, and negligible CH₄. Separating the produced CNF product from the gaseous effluents is straightforward due to the distinct phases of solid and gas, respectively. While separating H₂ from the gas stream, which primarily contains CO and CO₂, may pose a challenge, several commercialized separation techniques can be readily incorporated,

including pressure swing adsorption, cryogenic distillation, and membrane separation.^{48,49} The choice of the most suitable separation method for practical applications depends on various factors, such as the gas volume, required H₂ purity, energy efficiency, and cost considerations. Following the separation process, as postulated by the dashed lines in Fig. 4a, the remaining CO and CO₂, along with a minor amount of H₂O if any, can be directly recycled to the first electrolyzer for subsequent reactions. Moreover, control experiments where syngas is co-fed with water vapor or CO₂ into the thermal reactor show the potentially positive or neutral effects of recycling CO₂ and H₂O on the subsequent formation of CNF (see Supplementary Note 7, Supplementary Figs. 55 and 56).

Furthermore, we analyze energy consumption and net CO₂ emissions for our EC-TC system (See Supplementary Methods in SI, Supplementary Fig. 57a). Based on the laboratory-scale setup with a 10%Pd/C cathode in the electrolyzer at room temperature and the subsequent thermocatalytic reactor at 450 °C under ambient pressure, the total energy cost of the current EC-TC system is ~162 kWh/kg_{CNF}, lower than the reported value (~418 kWh/kg_{CNT}) for an electrochemical system operating at 750 °C for CO₂ fixation⁵⁰. Moreover, the EC-TC system produces an appreciable amount of H₂ and CO in addition to the solid carbon products, as well as O₂ reported in the precious electrochemical approaches. The current energy cost corresponds to net CO₂ emissions of ~56 kg_{CO2}/kg_{CNF}, which can be reduced to about 17 kg_{CO2}/kg_{CNF} with full integration of renewable energy for the electrochemical process. It is worth noting that future efforts can potentially achieve negative emissions with improvements, such as more efficient electrocatalysts and thermocatalysts, increased catalyst loading or densities, lower reaction temperatures, better insulation, and more renewable energy integration. Ideally, a negative emission of -3.67 kg_{CO2}/kg_{CNF} (Supplementary Fig. 57b) can be achieved if all EC-TC tandem processes are driven by renewable energy.

Conclusions

Numerous carbon dioxide (CO₂) transformation technologies generate end chemical products that re-emit CO₂ in their life cycle, making the CO₂ footprint of these processes at best carbon neutral. In contrast, results from the current study demonstrate a tandem electrochemical-thermochemical process to enable the fixation of CO₂ as valuable CNF at relatively mild conditions. By integrating a commercially available Pd/C electrocatalyst with a non-precious iron-cobalt (FeCo) thermocatalyst, we have achieved high quality CNF with an appreciable production rate (*avg.* 2.5 g_{carbon} g_{metals}⁻¹ h⁻¹) at ambient pressure. Combined reactor studies, *in situ* characterization and DFT calculations reveal the coordinated action of FeCo alloy with extra metallic Co as the highly active and selective catalyst for CO and H₂ dissociation, *O removal, and C-C bond formation in the CNF growth; moreover, the stable FeCo alloy demonstrates enhanced resistance to the formation of less active carbide species. Overall, by harnessing renewable energy and knowledge in thermocatalytic reactions, together with the implementation of product separation with metal recycling and an analysis of energy cost and CO₂ emissions, the tandem strategy represents a viable pathway to achieve negative carbon emissions while generating value-added solid carbon products and renewable H₂.

Methods

Catalysts Preparation for Thermochemical Reaction

All the catalysts for the thermochemical reaction were synthesized via a slurry impregnation method. For supported bimetallic catalysts, desired amounts of iron and cobalt nitrate precursors were dissolved in 30 ml of deionized (DI) water under stirring, followed by ultrasonication for 10 min. Afterwards, the support was added to the precursor solution under stirring with another 10 min of ultrasonication. The resulting liquid suspension was constantly stirred and dried at 70 °C overnight. The dried sample was ground into powder before being subject to calcination at 400 °C in static air for 2 h with a heating ramp rate of 1 °C min⁻¹. Following the same procedure, the monometallic catalysts were synthesized with the same total molar amount of metal elements as the bimetallic catalysts. Details about the precursors, metal loadings, atomic ratios, and support identity were specified in Supplementary Table 1.

Electrodes Preparation for Electrochemical Reaction

Commercial 10%Pd/C, 20%Pd/C, and 40%Pd/C (Vulcan carbon XC-72) catalysts were purchased from Fuel Cell Store and used without further purification. For cathode preparation, 60 mg of Pd/C powder was dispersed in a mixture containing 3 ml of isopropanol (Fisher Chemical), 1 ml of DI water, and 145 µl of 5% Nafion solution (Sigma Aldrich), followed by ultrasonication for 30 min. The resulting cathode ink was hand sprayed with an airbrush onto a carbon gas diffusion layer with a microporous layer (Sigracet 39BB, Fuel Cell Store) to obtain a mass loading of 1.0±0.1 mg cm⁻² after drying. Likewise, the anode was prepared by spraying the ink of IrO₂ (Alfa Aesar, Premion®, 99.99% (metals basis)) onto a platinized titanium fiber felt (Fuel Cell Store) with a mass loading of 3.0±0.1 mg cm⁻².

In situ X-Ray Diffraction (XRD)

The *in situ* time-resolved XRD measurements were performed at beamline 7-BM (QAS, 10¹² ph s⁻¹ @ 10 keV) of the National Synchrotron Light Source II (NSLS-II) at Brookhaven National Laboratory (BNL). A previously detailed Clausen cell⁵¹ equipped with a quartz capillary (1.2 mm O.D., 1.0 mm I.D.) was employed. For each *in situ* experiment, the sample (60-80 mesh) was fixed by two pieces of quartz wool and heated in a H₂/N₂ mixture (5/5 ml min⁻¹) from room temperature to 500 °C (or 700 °C) with a heating ramp rate of 10 °C min⁻¹ and held for 30 min. Afterwards, the sample was cooled down in the same atmosphere to 450 °C in 5 min before being exposed to the reaction stream (CO/H₂/N₂=3/3/4 ml min⁻¹) at 450 °C. For safety concerns, the reaction time was determined by the pressure build-up within the reactor. The energy of the incident X-ray was fixed and calibrated to the K-edge (20000 eV) of Mo foil, corresponding to a wavelength of 0.6199 Å. The two-dimensional (2D) diffraction images were continuously collected using a PerkinElmer 1621 area detector at a speed of one scan per 24 s. The sample-to-detector distance was calibrated by a CeO₂ standard. The 2D images were processed and integrated using the Dioptas software to obtain the XRD profiles after background subtraction.

In situ and ex situ X-Ray Absorption Spectroscopy (XAS)

The *in situ* and *ex situ* XAS measurements at the Fe K (7112 eV) and Co K (7709 eV) edges were conducted at beamlines 8-ID (ISS, 5×10¹³ ph s⁻¹ @ 10 keV) and 7-BM (QAS), respectively, at NSLS-II at BNL. Given the relatively low X-ray penetration depth at the 3d-metal energy, further attenuated by the CeO₂ support, the *in situ* XAS measurements were performed using a Nashner-Adler (N-A) reaction cell sealed by a Kapton window⁵². For each *in situ* measurement, an appropriate amount of fresh catalyst was pressed into a wafer (13 mm O.D.) and loaded into the

N-A cell. The sample was reduced by 50 vol% H₂ (H₂/N₂=20/20 ml min⁻¹) at 500 °C for 1 h. Afterwards, the sample was exposed to reaction stream (CO/H₂/N₂=15/15/20 ml min⁻¹) at 450 °C and held at 450 °C for 60 min. The XAS spectra were collected successively at a speed of 2 scans min⁻¹. Fe and Co foils were measured to calibrate the energy shifts as well as to obtain the passive factor (S_0^2) for the extended X-ray absorption fine structure (EXAFS) fittings. Other metal oxides (FeO, Fe₃O₄, Fe₂O₃, Co₃O₄, and CoO) were also measured for the sake of comparison with the X-ray absorption near edge structure (XANES) of different catalysts. For *ex situ* measurements, the spent catalysts were also pressed into a wafer (13 mm O.D.) and sealed by Kapton tapes. All data processing was performed using the IFEFFIT package.⁵³

Temperature-Programmed Reduction (TPR)

The TPR measurements were performed using an AMI-300ip (Altamira) instrument. For each test, approximately 50 mg of fresh catalyst was loaded in a U-shape quartz tube and pre-treated with He (50 ml min⁻¹) at 120 °C for 30 min in prior to cooling to 50 °C. Next, the sample was temperature-programmed (10 °C min⁻¹) heated to 850 °C in 10 vol% H₂ in Ar (50 ml min⁻¹). The hydrogen consumption profile as a function of reduction temperature was recorded via a thermal conductivity detector (TCD), which allowed to compare the reducibility of active metals in different catalysts.

Raman Spectroscopy

The structure of the carbon species on the spent catalysts was characterized using a Renishaw inVia Confocal Raman microscope with a 50× objective lens. The spent samples were excited by a 532 nm laser over the range of 270-2015 cm⁻¹. The spectral acquisition consisted of 10 scans with an exposure time of 10 s at 10% of maximum laser power. For the comparison of different samples, all the peak intensities were normalized to the intensity of the D band. To provide a reference for high-purity CNF, a commercial CNF product (C-GR-01-NFB, American Elements) was measured as well. More details can be referred to Supplementary Fig. 15 and Supplementary Table 4.

Inductively Coupled Plasma Optical Emission Spectroscopy (ICP-OES)

The ICP-OES analysis was conducted using an Agilent 5100 ICP-OES instrument on the liquid samples obtained after the separation process to determine the quantities of Fe and Co ions that had been leached out from the spent FeCo/CeO₂ catalysts.

Electron Microscopy

All the electron microscopy measurements were conducted using the facilities at the Center for Functional Nanomaterials (CFN) of BNL. Transmission electron microscopy (TEM) measurements were carried out using a JEOL 2100F (accelerating voltage of 200 kV) instrument. High-angle annular dark-field imaging (HAADF) imaging, energy-dispersive X-ray spectroscopy (EDS) mapping, and selected area electron diffraction (SAED) were carried out using an FEI Talos F200X S/TEM facility (accelerating voltage of 200 kV). Simultaneous high-resolution scanning electron microscopy (SEM) and ADF imaging were measured with a Hitachi 2700C STEM at an accelerating voltage of 200 kV. To prepare the sample, the catalyst powder was ultrasonically dispersed in ethanol for 3 min, after which a droplet was dripped onto a Lacey carbon film (300 mesh) supported on copper grids. After being dried at room temperature, the sample was used for measurements.

Thermochemical Evaluation

All the thermochemical experiments were conducted using a fixed-bed flow reactor (quartz tube, 7 mm ID, 9.6 mm OD) and heated by a Thermo Scientific Lindberg/Blue M furnace at ambient pressure. In each experiment, a desired amount of catalyst (60-80 mesh) was loaded into the quartz tube and secured by quartz wool on both sides. The catalyst was pre-reduced in 50 vol% H₂ in N₂ (total 40 ml min⁻¹) at 500 °C for 1 h before being cooled down to 450 °C in 15 min under the same atmosphere. Subsequently, the catalyst was exposed to the reaction stream of CO/H₂/N₂ with desired flow rates (3/3/4 ml min⁻¹) at 450 °C for different time on stream. The gas line connecting the reactor outlet to the gas chromatography (GC) inlet was maintained at 150 °C using heating tape to prevent the condensation of water vapor. To calibrate water vapor, a stable PtCo₃/CeO₂ catalyst was used to perform the reverse water-gas shift (RWGS) reaction at temperatures ranging from 150-350 °C.^{54,55} This produced a set of water vapor peak areas that were then correlated with their molar fractions, which were calculated based on the oxygen balance. The reactor effluents were analyzed using an Agilent 7890B GC equipped with PLOT Q and MOLESEIVE columns, as well as a TCD and a flame ionized detector (FID). N₂ was used as a balance gas to tune the inlet fraction of reactants and as an internal standard gas to correct for the volume-change effect due to the reaction. After the reaction, the catalyst was recollected from the tube reactor and weighed again. Reactant conversion (X), product selectivity (S), catalyst weight gain (CWG), and carbon balance (C_B) were calculated as follows:

$$X_i = \frac{F_{i,in} - F_{i,out}}{F_{i,in}} \times 100\% \quad (1)$$

$$S_{i \text{ in gas}} = \frac{n_i \times F_{i \text{ in gas,out}}}{\sum_i (n_i \times F_{i \text{ in gas,out}})} \times 100\% \quad (2)$$

$$S_{i \text{ in total}} = \frac{n_i \times F_{i \text{ in total,out}}}{F_{CO,in} - F_{CO,out}} \times 100\% \quad (3)$$

$$S_{C(s) \text{ in total}} = 1 - \frac{\sum_i (n_i \times F_{i \text{ in gas,out}})}{F_{CO,in} - F_{CO,out}} \times 100\% \quad (4)$$

$$CWG = m_{cat,spent} - m_{cat,fresh} \quad (5)$$

$$C_B = \frac{\sum_i n_i \times F_{i,out}}{F_{CO,in}} \times 100\% \quad (6)$$

where $F_{i,in}$ and $F_{i,out}$ referred to the N₂-corrected molar flow rates (μmol min⁻¹) of species i at the reactor inlet and outlet, respectively; $m_{cat,spent}$ and $m_{cat,fresh}$ represented the weight of the spent and fresh catalysts, respectively; n_i indicated the number of carbon in gaseous species i ; $S_{i \text{ in gas}}$ and $S_{i \text{ in total}}$ corresponded to the selectivity based on the gaseous C containing products (i.e., CO₂ and CH₄) and the total conversion of CO, respectively.

Electrochemical Evaluation

The CO₂ reduction reaction (CO₂RR) experiments were carried out using a zero-gap membrane electrode assembly (MEA) electrolyzer (5 cm², Dioxide Materials) with a stainless-steel cathode flow field and a titanium anode flow field. The cathodic flow field was fed with a CO₂/N₂ mixture (10/10 ml min⁻¹), while the anodic flow field was fed with a 50 mM KHCO₃ electrolyte at a flow rate of 5 ml min⁻¹ using a peristaltic pump. The cathode and anode compartments were separated by an anion exchange membrane (Sustainion X37-50 Grade RT, Dioxide Materials). The Pd/C cathode was pre-treated by being scanned between -0.05 V and -1.20 V (50 mV s⁻¹) for 20 cycles. Using linear sweep voltammetry (LSV), the cathode subsequently underwent scanning from 0 V to -3.00 V (20 mV s⁻¹) for two or three times to obtain a stable LSV. The chronopotentiometry tests under different constant current densities (-60, -100, -150, and -200 mA cm⁻²) were controlled

by a BioLogic VSP potentiostat complemented with a BioLogic VMP3B-20 (20 A/20 V) current booster, and the corresponding evolution of cell voltage was recorded. The cathodic effluents were directly analyzed by the same Agilent 7890B GC. The CO₂ conversion, H₂/CO ratio, and carbon balance were calculated based on equations (1) and (2), respectively.

$$X_{total} = \frac{F_{CO_2,in} - F_{CO_2,out}}{F_{CO_2,in}} \times 100\% \quad (7)$$

$$X_{product} = \frac{\sum_{i \neq CO_2} (n_i \times F_{i \text{ in gas, out}})}{F_{CO_2,in}} \times 100\% \quad (8)$$

$$X_{loss} = X_{total} - X_{product} \quad (9)$$

$$H_2/CO = \frac{F_{H_2,out}}{F_{CO,out}} \quad (10)$$

$$C_B = \frac{\sum_i (n_i \times F_{i \text{ in gas, out}})}{F_{CO_2,in}} \times 100\% \quad (11)$$

where the X_{total} , $X_{product}$, X_{loss} referred to the conversion based on the overall CO₂ consumption, the CO₂ converted into gaseous products, and the CO₂ lost to (bi)carbonate formation and crossover as well as liquid products, respectively.

Tandem Electrochemical-Thermochemical Evaluation

Evaluation of the tandem system was conducted using the same setups and procedures discussed earlier, except that the Fe₃Co₆/CeO₂ loading for the thermochemical reactor was 200 mg. The electrochemical reactor was carried out at -60, -100, -150, and -200 mA cm⁻² and the thermochemical reactor was maintained at 450 °C for about 11 h. The gaseous effluents from the MEA electrolyzer outlet were first passed through an ice trap and then directed to the inlet of the thermochemical reactor. Subsequently, all these gaseous effluents were analyzed using the Agilent 7890B GC. The total CO₂ conversion, fraction of CO₂ converted to gaseous products, CWG, and carbon balance were calculated based on equations (7), (8), (5), and (11), respectively. It should be noted that $S_{C(s) \text{ in total}}$ was not quantified due to the difficulty in simultaneously determining the CO₂ lost to (bi)carbonate formation and crossover and the CO₂ fixed in the solid carbon product.

CNF Separation and Catalyst Regeneration

The spent catalyst containing CNF was subject to ultrasonication in 5 mL of concentrated nitric acid (70%, 87.8 mmol) at room temperature for 30 min. The resulting suspension was refluxed under stirring at 120-130 °C for 2, 5, or 12 h. Afterwards, the suspension was cooled to room temperature and centrifuged at 4476 rcf (g) for 10 min; the transparent solution was decanted, while the wet powder was washed with 15 mL of DI water and sonicated for 5 min. The centrifugation and washing cycles were repeated three times. Subsequently, the wet powder was washed with 500 mL DI water and filtered using a PTFE membrane (pore size 0.1 μm), after which it was dried in vacuum at 80 °C overnight. All the solution containing iron and cobalt ions during centrifugation, washing, and filtration was collected and then concentrated at 80 °C for the next cycle of catalyst synthesis. For the synthesis of regenerated catalysts, an appropriate amount of new CeO₂ or dried solid products obtained after separation was added to the concentrated solution. The regenerated catalysts were subject to the same reduction treatment and reaction conditions as the fresh catalysts in the initial reactions. Similar methods can be referred to in Refs. 56 and 57.

Density Functional Theory (DFT) Calculations

Spin polarized DFT calculations^{58,59} were performed by using Vienna *ab initio* simulation package (VASP)⁶⁰. A 400eV kinetic energy cutoff and the projector augmented wave method (PAW)^{61,62} together with GGA exchange-correlation functional plus the PBE functional⁶³ were employed. The Van der Waals (VDW) force was addressed by using the DFT-D3 method developed by Grimme et al⁶⁴. Monkhorst-Pack⁶⁵ meshes were used to sample the Brillouin zone for all the surface calculations while gamma point were employed for all gas-phase species. The criteria for total energies and forces on all atoms were set as 10^{-6} eV and 0.02 eV \AA^{-1} for convergence, respectively. Methfessel-Paxton order one smearing with width 0.2 eV was used to improve the convergence. The Fe (3p, 3d, 4s), Co (3p, 3d, 4p), C (2s, 2p), O (2s, 2p) and H (1s) electrons were treated as valence states, while the remaining electrons were kept frozen as core states. The climbing image nudged elastic band method (CI-NEB)^{66,67} for each elementary reaction intermediates were conducted to derive the transition states. All the transition states have been verified with only one imaginary frequency by using harmonic approximation.

For the metallic bulk phases, body centered cubic (*bcc*) Fe and FeCo bulk phases and hexagonal close packed (*hcp*) Co bulk phase were used for bulk DFT calculations, where the optimized lattice parameters and the average magnetic moments are shown in Supplementary Fig. 23, consisting with the experimental values⁶⁸⁻⁷⁰. The most stable surfaces for *bcc* and *hcp* structures were adopted accordingly. Specifically, 3×3 Fe(110), 3×3 FeCo(110), and 4×4 Co(0001) surfaces with four layers (Supplementary Fig. 24) were used for surface DFT calculations with Monkhorst-Pack meshes of $3\times 2\times 1$, $3\times 2\times 1$, and $3\times 3\times 1$, respectively. As for the metal carbides, the Cementite-derived structures with orthorhombic system were adopted for Fe₃C, Co₃C, Fe₂CoC bulk phases, where the optimized lattice parameters and the magnetic moments per unit are also provided in Supplementary Fig. 25, consisting with the literature reports⁷¹⁻⁷³. According to previous studies on the stable surface and termination for metal carbides with Cementite-derived structures⁷⁴⁻⁷⁶, 2×1 Fe₃C(001), 2×1 Co₃C(001) and 2×1 Fe₂CoC(001) surfaces were adopted with Monkhorst-Pack meshes of $2\times 3\times 1$ (Supplementary Fig. 26). Fe₄/CeO₂(111), Fe₂Co₂/CeO₂(111), and Co₄/CeO₂(111) were used as simplified models to capture the metal-CeO₂ interaction at the interface (Supplementary Fig. 12). The Hubbard-like U term⁷⁷ with a value of 4.5 was applied for highly correlated Ce 4f states⁷⁸. A Gaussian smearing with a width of 0.05 eV was used to improve the convergence for all the CeO₂(111)-based models. The bottom O-Ce-O repetitive unit was fixed for all the CeO₂(111)-based calculations. The bottom two layers were fixed for the metallic surfaces and the bottom two Carbon-Metal-Metal-Carbon (C-M-M-C) repetitive units were fixed for the metal carbides while the rest of the atoms were allowed for full relaxation. The adsorption energy of adsorbate on each model surface was calculated as: $E_{\text{ads}} = E(\text{Adsorbate/Surface}) - E(\text{Surface}) - E(\text{Adsorbate})$.

Ab-initio Thermodynamic (AITD) Analysis

To explore the stabilities of metallic Fe, Co, FeCo alloy, and the corresponding carbides formation under the experimental reaction conditions, ab initio thermodynamics analysis was utilized⁷⁹⁻⁸¹, where two reactions (**R1** and **R2**) were considered as the extreme cases for the experimental processes without or with H₂ gas in the CO gas environment. Detailed derivations for the AITD analysis on monometallic, bimetallic, and carbides catalysts can be found in the Supplementary Information.

Data availability

The source data that support the findings of this study are available from the corresponding author on reasonable request. Source data are provided with this paper.

Acknowledgments:

This work was financially supported by the Division of Chemical Sciences, Geosciences, & Biosciences, Office of Basic Energy Sciences (grant number DE-SC0012704 and DE-FG02-13ER16381). This research used resources of the Center for Functional Nanomaterials (CFN) and beamlines 7-BM (QAS) and 8-ID (ISS) of the National Synchrotron Light Source II (NSLS-II) at Brookhaven National Laboratory (Contract No. DE-SC0012704 and DE-SC0012653), U.S. DOE Office of Science User Facilities. Beamline operations were supported in part by the Synchrotron Catalysis Consortium (U.S. DOE, Office of Basic Energy Sciences, Grant No. DE-SC0012335). The authors also acknowledge the assistance of Dr. Zhexi Lin, Amanda Ooi, and Danny Huang in performing Raman and ICP measurements. The DFT calculations were performed using computational resources at the Center for Functional Nanomaterials, a user facility at Brookhaven National Laboratory, and at the National Energy Research Scientific Computing Center (NERSC), which is supported by the Office of Science of the U.S. DOE under Contract No. DE-AC02-05CH11231. S.G. acknowledges the National Science Foundation Graduate Research Fellowship Program (DGE-2036197).

Author contributions:

Z.X., S.G. and J.G.C. conceived the idea and designed the research; Z.X. carried out catalyst synthesis, reactions, *in situ* synchrotron measurements, product separation, energy cost and CO₂ emission assessments, and analysis of all the experimental data; Z.X. and S.H. performed the electron microscopy imaging; S.G. contributed to the discussion, conducted Raman and ICP measurements, and assisted with the materials preparation and electrochemical experiments. E.H. conducted all the DFT calculations and theoretical data analysis under the supervision of P.L. and J.G.C.; Z.X. and E.H. prepared the initial draft; Z.X., E.H., S.G., P.L., and J.G.C. reviewed and revised the manuscript; and J.G.C. and P.L. supervised the whole project.

Competing interests declaration:

The authors declare that they have no competing interests.

Figure Legends/Captions

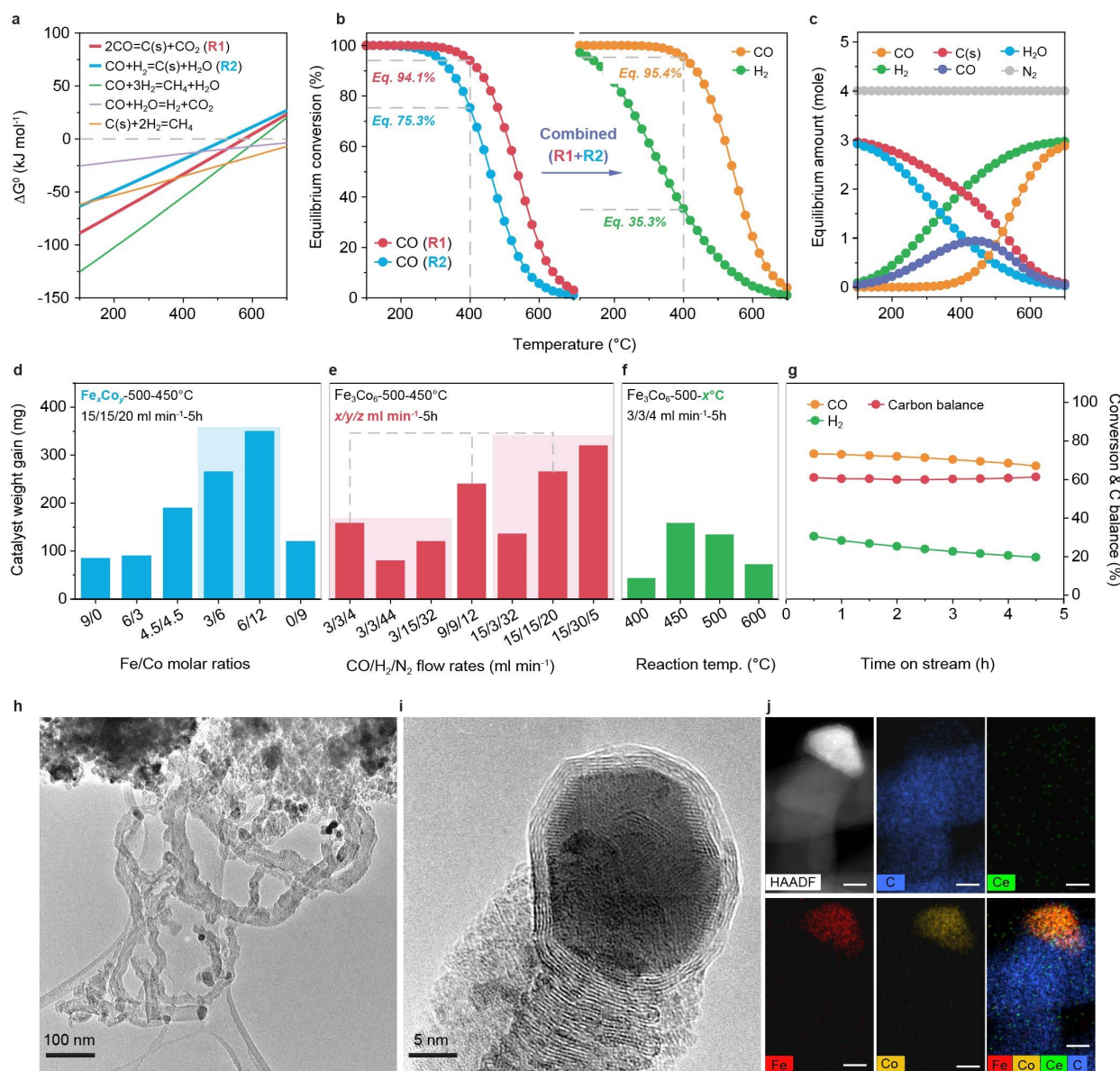


Fig. 1. Feasibility and demonstration of CNF formation from the CO and H₂ reaction. **a** Gibbs free energy change of primary reactions and potential side-reactions as a function of temperature. **b** Temperature dependence of equilibrium conversion of CO for individual **R1** ($2\text{CO}=\text{C}(\text{s})+\text{CO}_2$) and **R2** ($\text{CO}+\text{H}_2=\text{C}(\text{s})+\text{H}_2\text{O}$) reactions and of CO and H₂ in the presence of both **R1** and **R2**. **c** The corresponding equilibrium distribution of reactants (CO and H₂), products (C(s), CO₂, H₂O), and balance gas (N₂) for the right panel of Fig. 1B. **d-f** Effects of Fe/Co molar ratios, CO/H₂/N₂ flow rates, and reaction temperature on the catalyst weight gain after reaction, respectively. **(g)** Conversion of CO and H₂ as well as carbon balance over Fe₃Co₆/CeO₂ along time on stream at 450 °C. Approximately 100 mg of catalyst are used for each of the experiments shown in Figs. d-g. **h** Transmission electron microscopy (TEM) imaging of CNF over the spent Fe₃Co₆/CeO₂ catalyst. **i** High-resolution imaging of the tip of the resulting CNF. **j** Scanning transmission electron microscopy (STEM) high-angle annular dark field (HAADF) imaging and (energy-

dispersive X-ray spectroscopy) EDS mapping of C, Ce, Fe, and Co over the spent $\text{Fe}_3\text{Co}_6/\text{CeO}_2$ catalyst. The scale bar in each panel of Fig. 1j represents 8 nm.

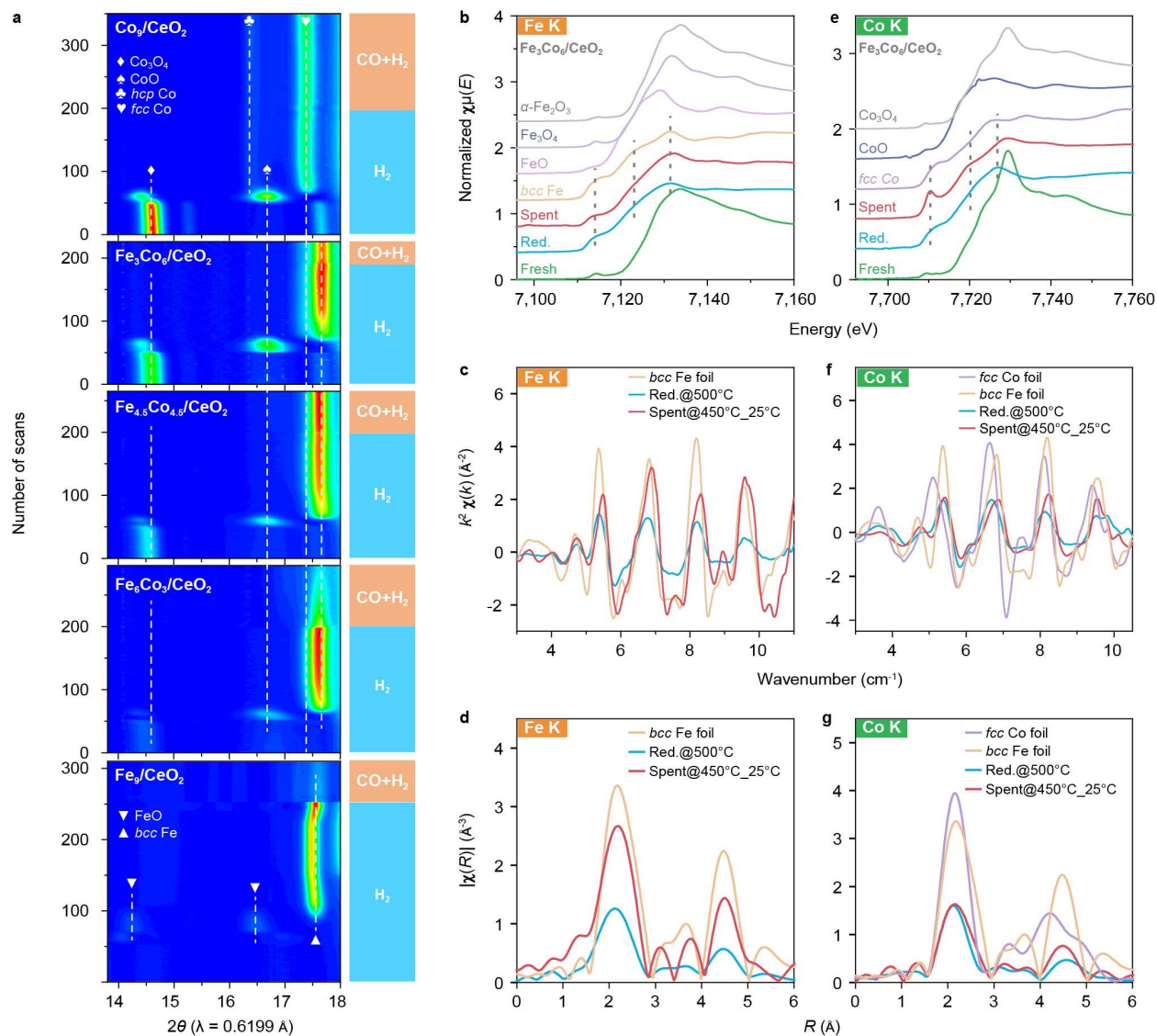


Fig. 2. *In situ* structural characterizations of CeO₂ supported FeCo-based catalysts. a *In situ* XRD patterns of Fe_xCo_y/CeO₂ catalysts ($x/y=0/9$, $3/6$, $4.5/4.5$, $6/3$, and $9/0$) under the reduction (H₂ only) and reaction (CO and H₂ at 450 °C) conditions. **b** The Fe K-edge XANES profile of Fe₃Co₆/CeO₂ under the fresh, reduction, and spent conditions as well as the reference standards (*bcc* Fe foil, FeO, Fe₃O₄, and Fe₂O₃). **c** and **d** The k^2 -weighted EXAFS of Fe K-edge in k space and R space, respectively, under the reduction and spent conditions as well as the *bcc* Fe foil. **e-g** The Co K-edge features of Fe₃Co₆/CeO₂ corresponding to the conditions in Figs. 2b-2d. Note: *Fresh* refers to exposure to N₂ at 25 °C; *Red.* represents reduction under H₂ at 500 °C; *Spent* indicates the catalyst was exposed to the reaction stream (CO and H₂) at 450 °C for about 5 h and then cooled down to room temperature for the XAFS measurement. More details about the peak assignment of XRD peaks can be found in Supplementary Fig. 22.

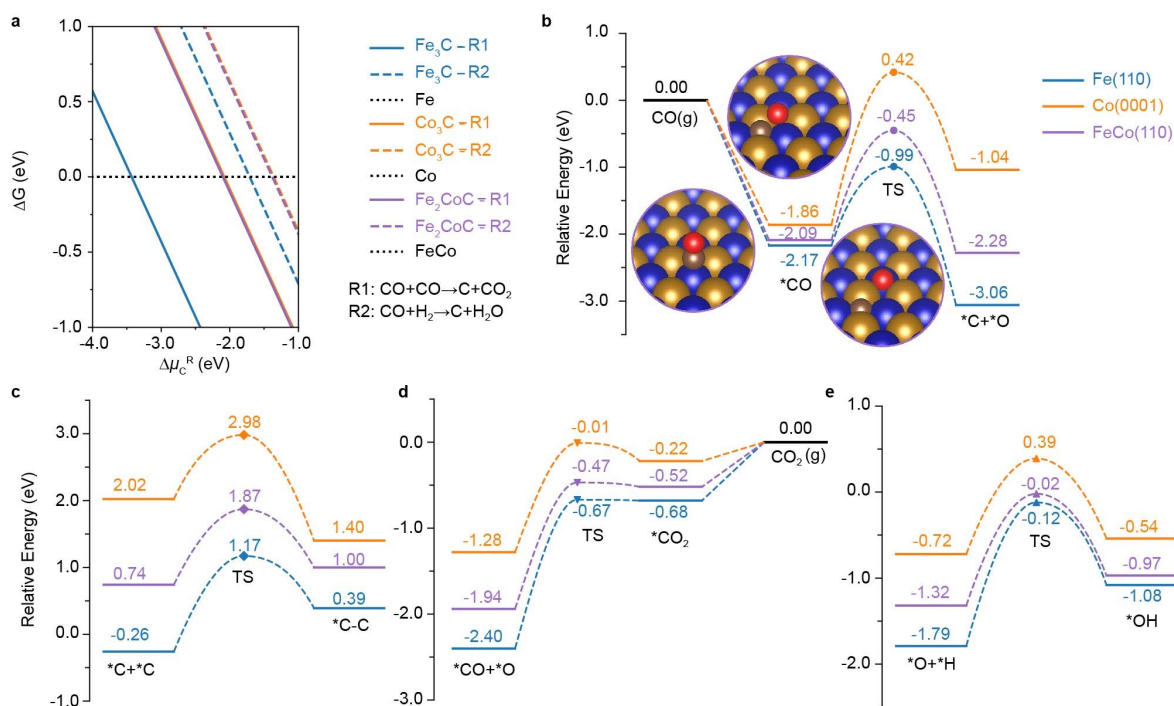


Fig. 3. Theoretical studies on the stability and reactivity of iron-cobalt catalysts. **a** *Ab initio* thermodynamic analysis for the stability of bulk phases (Fe, Co, FeCo, Fe₃C, Co₃C, Fe₂CoC) under the reaction conditions (P_{CO} and P_{H_2} : 0.1-1.0 bar; T : 325-525 °C). The corresponding chemical potential changes of C species at the reaction environments (P_{CO} and P_{H_2} : 0.1-1.0 bar; T : 325-525 °C) are shown in Supplementary Fig. 28. **b** DFT-calculated potential energy diagram for CO adsorption (*CO), dissociation (*C + *O) on Fe(110), Co(0001), and FeCo(110) surfaces. Inset: DFT-optimized structures for CO adsorption (*CO), dissociation (*C + *O) and corresponding transition state (TS) on FeCo(110) surfaces. **c** DFT-calculated potential energy diagram for C-C bond formation (*C + *C → *C-C) on Fe(110), Co(0001), and FeCo(110) surfaces. **d** DFT-calculated potential energy diagram for surface *O species removal in the form of CO₂ (*CO + *O → *CO₂ → CO₂) on Fe(110), Co(0001), and FeCo(110) surfaces. **e** DFT-calculated potential energy diagram for surface *O hydrogenation (*O + *H → *OH) on Fe(110), Co(0001) and FeCo(110) surfaces, followed by *H₂O formation via hydrogenation and removal in the form of H₂O. Yellow: Fe; Blue: Co; Brown: C; Red: O. The detailed top- and side-view structures can be found in Supplementary Figs. 29-35.

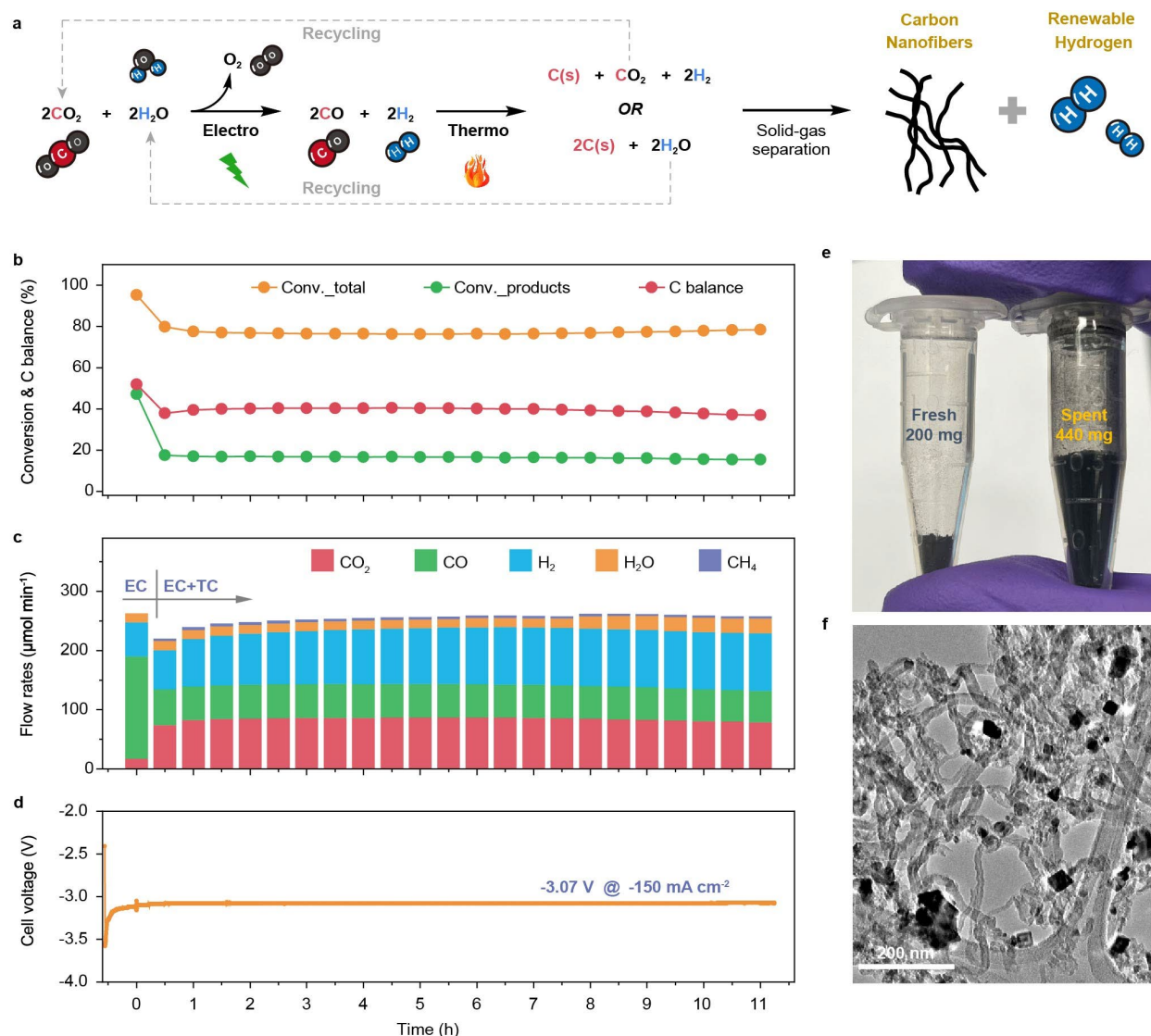


Fig. 4. Electrochemical-thermochemical tandem process for producing CNF and renewable H_2 . **a** Scheme of the electrochemical-thermochemical tandem process. **b-d** CO_2 conversion and carbon balance (b), molar flow rates of CO_2 , CO , H_2 , steam, and CH_4 during the tandem process (c), and cell voltage (d) at -150 mA cm^{-2} as a function of time. **e** Picture showing the fresh and spent $\text{Fe}_3\text{Co}_6/\text{CeO}_2$ catalysts for the tandem process. **f** TEM image of the resulting CNF after the ~11 h of tandem process. Reaction conditions: 1 atm, electrolyzer ($10\% \text{Pd/C}$, 1 mg cm^{-2} , $\text{CO}_2/\text{N}_2=10/10 \text{ ml min}^{-1}$, -150 mA cm^{-2} , $25 \text{ }^\circ\text{C}$), and thermal reactor ($\text{Fe}_3\text{Co}_6/\text{CeO}_2$, 200 mg , $450 \text{ }^\circ\text{C}$). Notes: *Conv._total* and *Conv._products* refer to the CO_2 conversion based on total CO_2 consumption (X_{total}) and carbon-containing gaseous products (X_{products}), respectively; *EC* and *TC* represent electrochemical and thermochemical reactors, respectively; given safety concerns, the reaction is stopped at 11 h because of the severe blockage of the thermal reactor caused by CNF growth.

References

1. Armstrong McKay, D. I. *et al.* Exceeding 1.5°C global warming could trigger multiple climate tipping points. *Science* **377**, eabn7950 (2022).
2. Matthews, H. D. & Wynes, S. Current global efforts are insufficient to limit warming to 1.5°C. *Science* **376**, 1404–1409 (2022).
3. Chen, S., Liu, J., Zhang, Q., Teng, F. & McLellan, B. C. A critical review on deployment planning and risk analysis of carbon capture, utilization, and storage (CCUS) toward carbon neutrality. *Renew. Sust. Energ. Rev.* **167**, 112537 (2022).
4. Wang, D., Xie, Z., Porosoff, M. D. & Chen, J. G. Recent advances in carbon dioxide hydrogenation to produce olefins and aromatics. *Chem* **7**, 2277–2311 (2021).
5. Jiang, X., Nie, X., Guo, X., Song, C. & Chen, J. G. Recent Advances in Carbon Dioxide Hydrogenation to Methanol via Heterogeneous Catalysis. *Chem. Rev.* **120**, 7984–8034 (2020).
6. Xie, Z. & Chen, J. G. Bimetallic-Derived Catalytic Structures for CO₂-Assisted Ethane Activation. *Acc. Chem. Res.* (2023) doi:10.1021/acs.accounts.3c00348.
7. De Luna, P. *et al.* What would it take for renewably powered electrosynthesis to displace petrochemical processes? *Science* **364**, eaav3506 (2019).
8. Ge, L. *et al.* Electrochemical CO₂ reduction in membrane-electrode assemblies. *Chem* **8**, 663–692 (2022).
9. She, X., Wang, Y., Xu, H., Chi Edman Tsang, S. & Ping Lau, S. Challenges and Opportunities in Electrocatalytic CO₂ Reduction to Chemicals and Fuels. *Angew. Chem. Int. Ed.* **61**, e202211396 (2022).
10. Jin, J. *et al.* Constrained C₂ adsorbate orientation enables CO-to-acetate electroreduction. *Nature* **617**, 724–729 (2023).
11. Lin, H., Luo, S., Zhang, H. & Ye, J. Toward solar-driven carbon recycling. *Joule* **6**, 294–314 (2022).
12. Biswas, A. N. *et al.* Oxygenate Production from Plasma-Activated Reaction of CO₂ and Ethane. *ACS Energy Lett.* **7**, 236–241 (2022).
13. George, A. *et al.* A Review of Non-Thermal Plasma Technology: A novel solution for CO₂ conversion and utilization. *Renew. Sust. Energ. Rev.* **135**, 109702 (2021).
14. Wang, Q., Kalathil, S., Pornrungrroj, C., Sahm, C. D. & Reisner, E. Bacteria–photocatalyst sheet for sustainable carbon dioxide utilization. *Nat. Catal.* **5**, 633–641 (2022).
15. Schwarz, F. M., Moon, J., Oswald, F. & Müller, V. Biological hydrogen storage and release through multiple cycles of bi-directional hydrogenation of CO₂ to formic acid in a single process unit. *Joule* **6**, 1304–1319 (2022).
16. Biswas, A. N., Winter, L. R., Xie, Z. & Chen, J. G. Utilizing CO₂ as a Reactant for C₃ Oxygenate Production via Tandem Reactions. *JACS Au* **3**, 293–305 (2023).
17. Lee, M. G. *et al.* Selective synthesis of butane from carbon monoxide using cascade electrolysis and thermocatalysis at ambient conditions. *Nat. Catal.* **6**, 310–318 (2023).
18. Anderson, K. & Peters, G. The trouble with negative emissions. *Science* **354**, 182–183 (2016).

19. Biniek, K., Henderson, K., Rogers, M. & Santoni, G. Driving CO₂ emissions to zero (and beyond) with carbon capture, use, and storage. *McKinsey Quarterly* (2020).
20. *Global Carbon Nano Materials Market By Product Type: Global Opportunity Analysis and Industry Forecast, 2021-2031*. (2022).
21. Esrafilzadeh, D. *et al.* Room temperature CO₂ reduction to solid carbon species on liquid metals featuring atomically thin ceria interfaces. *Nat. Commun.* **10**, 1–8 (2019).
22. Zuraiqi, K. *et al.* Direct conversion of CO₂ to solid carbon by Ga-based liquid metals. *Energy Environ. Sci.* **15**, 595–600 (2022).
23. Ye, L. *et al.* Low-Temperature CO₂ Reduction using Mg–Ga Liquid Metal Interface. *Adv. Mater. Interfaces* **10**, 2201625 (2023).
24. Ren, J., Li, F.-F., Lau, J., González-Urbina, L. & Licht, S. One-Pot Synthesis of Carbon Nanofibers from CO₂. *Nano Lett.* **15**, 6142–6148 (2015).
25. Wu, H. *et al.* One-pot synthesis of nanostructured carbon materials from carbon dioxide via electrolysis in molten carbonate salts. *Carbon* **106**, 208–217 (2016).
26. Ruiz-Cornejo, J. C., Sebastián, D. & Lázaro, M. J. Synthesis and applications of carbon nanofibers: a review. *Rev. Chem. Eng.* **36**, 493–511 (2020).
27. Shi, T., Li, Z., Guo, J., Gong, H. & Gu, C. Research progress on CNTs/CNFs-modified cement-based composites – A review. *Constr. Build. Mater.* **202**, 290–307 (2019).
28. Metaxa, Z. S., Konsta-Gdoutos, M. S. & Shah, S. P. Carbon nanofiber–reinforced cement-based materials. *Transp. Res. Rec.* **2142**, 114–118 (2010).
29. Ilinova, A. & Kuznetsova, E. CC(U)S initiatives: Prospects and economic efficiency in a circular economy. *Energy Rep.* **8**, 1295–1301 (2022).
30. Sharma, R. & Kar, K. K. Characteristics of carbon nanofibers. *Handbook of Nanocomposite Supercapacitor Materials I: Characteristics* 215–245 (2020).
31. Annesini, M. C., Piemonte, V. & Turchetti, L. Carbon formation in the steam reforming process: a thermodynamic analysis based on the elemental composition. *Chem. Eng. Trans.* **11**, (2007).
32. Alipour, Z., Babu Borugadda, V., Wang, H. & Dalai, A. K. Syngas production through dry reforming: A review on catalysts and their materials, preparation methods and reactor type. *Chem. Eng. J.* **452**, 139416 (2023).
33. Rodriguez, N. M. A review of catalytically grown carbon nanofibers. *J. Mater. Res.* **8**, (1993).
34. Xie, Z., Winter, L. R. & Chen, J. G. Bimetallic-Derived Catalysts and Their Application in Simultaneous Upgrading of CO₂ and Ethane. *Matter* **4**, 408–440 (2021).
35. Fan, H. *et al.* Dynamic State and Active Structure of Ni–Co Catalyst in Carbon Nanofiber Growth Revealed by *in Situ* Transmission Electron Microscopy. *ACS Nano* **15**, 17895–17906 (2021).
36. Young, D. J., Zhang, J., Geers, C. & Schütze, M. Recent advances in understanding metal dusting: A review. *Mater. Corros.* **62**, 7–28 (2011).

37. Guo, X., Vullum, P. E. & Venvik, H. J. Inhibition of metal dusting corrosion on Fe-based alloy by combined near surface severe plastic deformation (NS-SPD) and thermochemical treatment. *Corros. Sci.* **190**, 109702 (2021).
38. Khadra, G. *et al.* Structure and Magnetic Properties of FeCo Clusters: Carbon Environment and Annealing Effects. *J. Phys. Chem. C* **121**, 10713–10718 (2017).
39. Carta, D., Mountjoy, G., Apps, R. & Corrias, A. Effect of the Support on the Formation of FeCo Alloy Nanoparticles in an SBA-16 Mesoporous Silica Matrix: An X-ray Absorption Spectroscopy Study. *J. Phys. Chem. C* **116**, 12353–12365 (2012).
40. Van Ravenhorst, I. K. *et al.* On the Cobalt Carbide Formation in a Co/TiO₂ Fischer–Tropsch Synthesis Catalyst as Studied by High-Pressure, Long-Term *Operando* X-ray Absorption and Diffraction. *ACS Catal.* **11**, 2956–2967 (2021).
41. Liu, P. & Nørskov, J. K. Ligand and ensemble effects in adsorption on alloy surfaces. *Phys. Chem. Chem. Phys.* **3**, 3814–3818 (2001).
42. Rodriguez, J. The chemical properties of bimetallic surfaces: Importance of ensemble and electronic effects in the adsorption of sulfur and SO₂. *Prog. Surf. Sci.* **81**, 141–189 (2006).
43. Ozden, A. *et al.* Carbon-efficient carbon dioxide electrolyzers. *Nat. Sustain.* **5**, 563–573 (2022).
44. Li, H. *et al.* Tailoring acidic microenvironments for carbon-efficient CO₂ electrolysis over a Ni–N–C catalyst in a membrane electrode assembly electrolyzer. *Energy Environ. Sci.* **16**, 1502–1510 (2023).
45. Nitopi, S. *et al.* Progress and Perspectives of Electrochemical CO₂ Reduction on Copper in Aqueous Electrolyte. *Chem. Rev.* **119**, 7610–7672 (2019).
46. Saha, P., Amanullah, S. & Dey, A. Selectivity in Electrochemical CO₂ Reduction. *Acc. Chem. Res.* **55**, 134–144 (2022).
47. Sheng, W. *et al.* Electrochemical reduction of CO₂ to synthesis gas with controlled CO/H₂ ratios. *Energy Environ. Sci.* **10**, 1180–1185 (2017).
48. Cavaliere, P. Hydrogen Separation and Purification. in *Water Electrolysis for Hydrogen Production* (ed. Cavaliere, P.) 509–541 (Springer International Publishing, 2023). doi:10.1007/978-3-031-37780-8_14.
49. Du, Z. *et al.* A Review of Hydrogen Purification Technologies for Fuel Cell Vehicles. *Catalysts* **11**, 393 (2021).
50. Douglas, A., Carter, R., Li, M. & Pint, C. L. Toward Small-Diameter Carbon Nanotubes Synthesized from Captured Carbon Dioxide: Critical Role of Catalyst Coarsening. *ACS Appl. Mater. Interfaces* **10**, 19010–19018 (2018).
51. Chupas, P. J. *et al.* A versatile sample-environment cell for non-ambient X-ray scattering experiments. *J. Appl. Crystallogr.* **41**, 822–824 (2008).
52. Marinkovic, N. S., Ehrlich, S. N., Northrup, P., Chu, Y. & Frenkel, A. I. Synchrotron Catalysis Consortium (SCC) at NSLS-II: Dedicated Beamline Facilities for In Situ and Operando Characterization of Catalysts. *Synchrotron Radiat. News* **33**, 4–9 (2020).
53. Ravel, B. & Newville, M. ATHENA, ARTEMIS, HEPHAESTUS: data analysis for X-ray absorption spectroscopy using IFEFFIT. *J. Synchrotron Radiat.* **12**, 537–541 (2005).

54. Xie, Z. *et al.* Reactions of CO₂ and ethane enable CO bond insertion for production of C₃ oxygenates. *Nat. Commun.* **11**, 1887 (2020).
55. Xie, Z., Wang, X., Chen, X., Liu, P. & Chen, J. G. General Descriptors for CO₂-Assisted Selective C–H/C–C Bond Scission in Ethane. *J. Am. Chem. Soc.* **144**, 4186–4195 (2022).
56. Dujardin, E., Ebbesen, T. W., Krishnan, A. & Treacy, M. M. J. Purification of Single-Shell Nanotubes. *Adv. Mater.* **10**, 611–613 (1998).
57. Wang, I.-W. *et al.* Catalytic decomposition of methane into hydrogen and high-value carbons: combined experimental and DFT computational study. *Catal. Sci. Technol.* **11**, 4911–4921 (2021).
58. Hohenberg, P. & Kohn, W. Inhomogeneous electron gas. *Phys. Rev.* **136**, B864–B871 (1964).
59. Kohn, W. & Sham, L. J. Self-consistent equations including exchange and correlation effects. *Phys. Rev.* **140**, A1133–A1138 (1965).
60. Kresse, G. & Furthmüller, J. Efficient iterative schemes for ab initio total-energy calculations using a plane-wave basis set. *Phys. Rev. B* **54**, 11169–11186 (1996).
61. Blochl, P. E. Projector augmented-wave method. *Phys. Rev. B* **50**, 17953–17979 (1994).
62. Kresse, G. & Joubert, D. From ultrasoft pseudopotentials to the projector augmented-wave method. *Phys. Rev. B* **59**, 1758–1775 (1999).
63. Perdew, J. P., Burke, K. & Ernzerhof, M. Generalized gradient approximation made simple. *Phys. Rev. Lett.* **77**, 3865–3868 (1996).
64. Grimme, S., Antony, J., Ehrlich, S. & Krieg, H. A consistent and accurate ab initio parametrization of density functional dispersion correction (DFT-D) for the 94 elements H–Pu. *J. Chem. Phys.* **132**, 154104 (2010).
65. Monkhorst, H. J. & Pack, J. D. Special points for Brillouin-zone integrations. *Phys. Rev. B* **13**, 5188–5192 (1976).
66. Henkelman, G. & Jonsson, H. Improved tangent estimate in the nudged elastic band method for finding minimum energy paths and saddle points. *J. Chem. Phys.* **113**, 9978–9985 (2000).
67. Henkelman, G., Uberuaga, B. P. & Jonsson, H. A climbing image nudged elastic band method for finding saddle points and minimum energy paths. *J. Chem. Phys.* **113**, 9901–9904 (2000).
68. Moruzzi, V. L., Marcus, P. M., Schwarz, K. & Mohn, P. Ferromagnetic phases of bcc and fcc Fe, Co, and Ni. *Phys. Rev. B* **34**, 1784–1791 (1986).
69. Liu, A. Y. & Singh, D. J. General-potential study of the electronic and magnetic structure of FeCo. *Phys. Rev. B* **46**, 11145–11148 (1992).
70. Li, C., Freeman, A. J. & Fu, C. L. Electronic structure and magnetic properties of the hcp Co(0001) surface. *J. Magn. Magn. Mater.* **94**, 134–140 (1991).
71. Faraoun, H. I., Zhang, Y. D., Esling, C. & Aourag, H. Crystalline, electronic, and magnetic structures of θ -Fe₃C, χ -Fe₅C₂, and η -Fe₂C from first principle calculation. *J. Appl. Phys.* **99**, (2006).
72. Gao, Y. *et al.* First-principles study on surface structural, magnetic and electronic properties of alloyed cementite with Co or Ni. *Comput. Mater. Sci.* **85**, 154–158 (2014).

73. Shein, I. R., Medvedeva, N. I. & Ivanovskii, A. L. Electronic and structural properties of cementite-type M_3X ($M=Fe, Co, Ni$; $X=C$ or B) by first principles calculations. *Phys. B: Condens. Matter* **371**, 126–132 (2006).
74. Chiou, W. C. & Carter, E. A. Structure and stability of Fe_3C -cementite surfaces from first principles. *Surf. Sci.* **530**, 88–100 (2003).
75. Broos, R. J. P., Klumpers, B., Zijlstra, B., Filot, I. A. W. & Hensen, E. J. M. A quantum-chemical study of the CO dissociation mechanism on low-index Miller planes of Θ - Fe_3C . *Catal. Today* **342**, 152–160 (2020).
76. Shen, X. *et al.* Carburized cobalt catalyst for the Fischer–Tropsch synthesis. *Catal. Sci. Technol.* **11**, 6564–6572 (2021).
77. Dudarev, S. L., Botton, G. A., Savrasov, S. Y., Humphreys, C. J. & Sutton, A. P. Electron-energy-loss spectra and the structural stability of nickel oxide: An LSDA+U study. *Phys. Rev. B* **57**, 1505–1509 (1998).
78. Liu, Z. *et al.* Water-promoted interfacial pathways in methane oxidation to methanol on a CeO_2 - Cu_2O catalyst. *Science* **368**, 513–517 (2020).
79. Reuter, K. & Scheffler, M. Composition, structure, and stability of $RuO_2(110)$ as a function of oxygen pressure. *Phys. Rev. B* **65**, 035406 (2001).
80. Reuter, K. & Scheffler, M. Composition and structure of the $RuO_2(110)$ surface in an O_2 and CO environment: Implications for the catalytic formation of CO_2 . *Phys. Rev. B* **68**, 045407 (2003).
81. Kang, J. *et al.* Surface characterization and methane activation on $SnO_x/Cu_2O/Cu(111)$ inverse oxide/metal catalysts. *Phys. Chem. Chem. Phys.* **23**, 17186–17196 (2021).